Biocompatible CuO-decorated carbon nanoplatforms for multiplexed imaging and enhanced antitumor efficacy *via* combined photothermal therapy/chemodynamic therapy/chemotherapy

Fan Jiang[1,2], Binbin Ding[1,2], Yajie Zhao[1,2], Shuang Liang[1,2], Ziyong Cheng[1,2], Bengang Xing[3], Bo Teng[4], Ping'an Ma[1,2*] and Jun Lin[1,2*]

ABSTRACT   Inspired by the limitations of nanoparticles in cancer treatment caused by their low therapeutic effects and biotoxicity, biocompatible and photothermal enhanced copper oxide-decorated carbon nanospheres (CuO@CNSs) with doxorubicin hydrochloride (DOX) loading were constructed. CNSs as photothermal agents were synthesized by a hydrothermal reaction. CuO was adsorbed on the surface of CNSs, which improved the photothermal conversion efficiency due to the electron transitions between C-2p and Cu-3d. In addition, CuO would release Cu^{2+} ions in the tumor microenvironment, which could produce hydroxyl radical (·OH) to induce cancer cells apoptosis *via* Haber-Weiss and Fenton-like reactions. DOX as a chemotherapeutic agent was located on the surface of CuO@CNSs by electrostatic adsorption and released quickly in the tumor microenvironment to kill cancer cells. The CuO@CNSs-DOX nanoplatforms realized the combination therapy of photothermal therapy (PTT), chemodynamic therapy (CDT), and chemotherapy (CT), which have strong potential for cancer treatment.

Keywords: CuO, carbon nanospheres, enhanced photothermal therapy, chemodynamic therapy, chemotherapy

INTRODUCTION

Cancer is a serious threat to human health. Chemotherapy (CT) is considered to be the most commonly used treatment. However, CT has many disadvantages such as drug resistance and severe side effects, which limit its wide-spread use [1,2]. Photothermal therapy (PTT) has attracted much attention worldwide due to its low cost and ignorable side effect [3–5]. Upon near-infrared (NIR) irradiation, photothermal reagents can rapidly convert light into heat to kill cancer cells through hyperthermia. Carbon-based materials [6–9] exhibit great potential as photothermal agents because of their unique optical features, good biocompatibility, and low biotoxicity. However, the therapeutic effect of carbon-based materials is hindered due to the low photothermal conversion efficiency.

Chemodynamic therapy (CDT) has been widely studied recently. A large amount of hydroxyl radicals (·OH) could be produced to accelerate cancer cell apoptosis *via* the reaction between the tumor microenvironment and CDT agent. Some metal (iron [10–12], copper [10,13–15], manganese [16–18], silver [17,19]) ions have been reported to produce ·OH by catalyzing hydrogen peroxide in the tumor microenvironment. For instance, our group [16] developed a nanoplatform with *in-situ* growth of MnO_2 on the surfaces of upconversion nanoparticles (UCNPs). MnO_2 released Mn^{2+} in the tumor microenvironment, and the released Mn^{2+} can produce ·OH by a Fenton-like reaction. However, as the reaction proceeds, the H_2O_2 content in the microenvironment decreases and the therapeutic effect is limited. Therefore, to solve this problem and achieve the best therapeutic effect, combination therapy has proved to be an attractive strategy.

Among various combination treatments, the combina-

---

[1] State Key Laboratory of Rare Earth Resource Utilization, Changchun Institute of Applied Chemistry, Chinese Academy of Sciences, Changchun 130022, China
[2] University of Science and Technology of China, Hefei 230026, China
[3] School of Physical & Mathematical Sciences, Nanyang Technological University, Singapore
[4] Department of Otolaryngology Head and Neck Surgery, The Second Hospital, Jilin University, Changchun 130041, China
* Corresponding authors (emails: mapa675@ciac.ac.cn (Ma P); jlin@ciac.ac.cn (Lin J))

tion of PTT, CDT and CT multi-mode treatment platforms has attracted much attention [20,21]. Multifunctional nanoplatforms DOX@Fe(III)@WS$_2$-PVP (DOX, doxorubicin hydrochloride; PVP, polyvinylpyrrolidone) were synthesized by Wu *et al.* [22]. WS$_2$ acted as a photothermal agent. Fe(III) reacted with WS$_2$ to form Fe^{2+} and WO$_4^{2-}$, and then Fe^{2+} catalyzed H$_2$O$_2$ in tumor cells to produce ·OH *via* the Fenton reaction. DOX was released rapidly at the tumor site. Magnetic Co$_3$O$_4$-DOX was also synthesized for multi-mode theranostics of cancer [23]. Co$_3$O$_4$ acted as the photothermal agent and released Co^{3+} to produce ·OH in the tumor microenvironment. DOX was also released at the same time to kill tumor cells. In brief, the multi-mode treatment platforms have been proved to exhibit excellent anticancer efficacy.

Here we designed multifunctional nanoplatforms CuO@CNSs-DOX (CNSs=carbon nanospheres) to realize the combination therapy of PTT, CDT, and CT. To our knowledge, it is the first report on integrating semiconductor CuO and biocompatible CNSs into CuO@CNSs nanocomposites for cancer treatment. CNSs as photothermal agents were prepared by hydrothermal reaction [24]. CuO was adsorbed on the surface of CNSs, which not only served as a CDT agent but also improved the photothermal conversion efficiency of nanoparticles. DOX was loaded on the surface of CuO@CNSs by electrostatic adsorption and released at the tumor site. Besides, CuO@CNSs can be used for infrared (IR) thermal imaging and photoacoustic (PA) imaging, which provided the real-time diagnosis for diseases [25,26]. The multifunctional nanoplatforms have good antitumor effect *in vitro* and *in vivo*, which are promising to be used in cancer treatment.

EXPERIMENTAL SECTION

Preparation of CNSs and CuO@CNSs
The CNSs were prepared *via* a hydrothermal method [24]. In a nutshell, glucose was dissolved in deionized water. The mixture were transformed into an autoclave and maintained at 180°C for 6 h. The products were separated by centrifugation and dried in vacuum at 60°C.

For obtaining CuO@CNSs, CNSs (0.1 g) were dispersed in 5 mL of water, and CuCl$_2$·2H$_2$O (0.0862 g) was added into the solution and stirred at room temperature for 4 h. The CuO@CNSs were centrifuged at 10,000 r min^{-1} for 10 min and washed with ethanol and water. The products were dried in vacuum at 60°C.

The release of Cu^{2+} from CuO@CNSs
CuO@CNSs (5 mg) were dispersed in 2 mL of phosphate buffer saline (PBS) with different pH (7.4, 6.5 and 5.0) at a certain amount of time. The supernatants were obtained by centrifugation and replaced by the same amount of fresh PBS solution. The mass of released Cu^{2+} ions was tested by inductively coupled plasma mass spectrometry (ICP-MS).

Extracellular ·OH detection
NaOH (0.4 g) was dissolved in 50 mL of deionized water to form a transparent solution. Then 0.8307 g terephthalic acid (TAOH) was added to form a homogeneous solution. The fluorescence at 430 nm of the solution (H$_2$O +TAOH, TAOH+8 mmol L^{-1} H$_2$O$_2$, CuO@CNSs+TAOH, CuO@CNSs+TAOH+8 mmol L^{-1} H$_2$O$_2$) was determined using an F7000 fluorescence spectrometer after removal of the nanoparticles by centrifugation.

To assess the connection between the amount of produced ·OH and the concentration of H$_2$O$_2$, different concentrations of H$_2$O$_2$ (0, 2, 4, 8, and 16 mmol L^{-1}) were mixed with CuO@CNSs (200 ppm). The fluorescence of the solution at 430 nm was observed after removal of the nanoparticles by centrifugation.

To assess the connection between the amount of produced ·OH and pH of the environment, CuO@CNSs (2 mg) were dispensed in PBS (pH 7.4, 6.5 and 5.0), and then TAOH was added into the solution. The fluorescence of the mixture at 430 nm was observed after removal of the nanoparticles by centrifugation.

Intracellular ·OH detection
4T1 cells were seeded on 12-well plates at a density of 6×10^4 cells per well and treated with (i) Control; (ii) CNSs; (iii) CuO@CNSs. After incubation at 37°C for 4 h, the cells were washed with PBS, and ROS probe was added to each well and incubated at 37°C for 30 min. Finally, the cells were washed with PBS and observed by a florescence microscope system (Nikon Ti-S).

Photothermal properties
CuO@CNSs (0, 50, 100, 200, 400, and 800 ppm, 0.2 mL) were exposed to the 808-nm NIR laser (2 W cm^{-2}) for 10 min in 96-well plates, an IR thermal camera (S6-a, IRS, China) was used to record the change of temperature. In addition, CuO@CNSs solutions were irradiated by 808-nm NIR laser (2 W cm^{-2}) for 5 min and cooled for 5 min, and the process lasted five cycles to investigate the photothermal stability.

Photothermal conversion efficiency
CuO@CNSs solution (200 ppm, 1 mL) was added in a

cuvette and irradiated by NIR laser (808 nm, 2 W cm^{-2}, 10 min), and then naturally cooled for another 10 min. The change of temperature was recorded every 30 s. The photothermal conversion efficiency of aqueous CNSs solution (1 mL, 200 ppm) was measured in the same way.

Live/dead cell staining
Calcein-AM and propidium iodide (PI) were used to assess the photothermal performance. 4T1 cells were incubated with CuO@CNSs (0, 25, 50, 100, and 200 ppm) and exposed to NIR laser irradiation (808 nm, 2 W cm^{-2}, 10 min), and then the cells were co-stained with Calcein AM (green, live cells) and PI following the manufacturer's instructions (BestBio, Shanghai, China).

Computational details
The calculations were based on density functional theory (DFT) with the Perdew-Burke-Ernzerbof (PBE) form of generalized gradient approximation functional (GGA). The Vienna *Ab-Initio* Simulation Package (VASP) was employed. The cut off of plane wave energy was set as 400 eV. The Fermi scheme was shown for electron occupancy with an energy smearing of 0.1 eV. The energy and force were set as 1.0×10^{-6} eV/atom and 0.01 eV Å^{-1}, respectively for geometry optimization. All calculations included the spin polarization.

Loading of DOX
CuO@CNSs (5 mg) were dispersed in 2 mL of deionized water and mixed with 2 mL of DOX solution (1 mg mL^{-1}). The solution was stirred for 24 h in dark. Then CuO@CNSs-DOX was obtained by centrifugation. The supernatant was collected and tested by ultraviolet-visible (UV-Vis) spectrometry. Loading efficiency of DOX was calculated by using the following equation:
loading efficiency=(weight of loaded DOX)/(weight of (loaded DOX+CuO@CNSs))×100%.

Release behavior of DOX
CuO@CNSs-DOX (5 mg) were dispensed in 2 mL of PBS (pH 7.4, 6.5, and 5.0), and the solution was shaken slightly at 37°C.

To explore the photothermal-triggered DOX release, the solution was irradiated by 808-nm NIR laser for 10 min at specific time points. The supernatants were obtained by centrifugation and the absorbance at the wavelength of 480 nm was measured by UV-Vis spectrometry.

Cellular uptake
4T1 cells were seeded into 12-well plates (1×10^4 cells per well) and incubated with CuO@CNSs-DOX for different times (10 min, 1 and 4 h), and then the fluorescence microscope was used for cell imaging. ICP-MS was also used to detect the cellular uptake. 4T1 cells were seeded in 6-well plates (3×10^5 cells per well) and cultured with CuO@CNSs at 37°C for 10 min, 1 and 4 h, respectively. The cells were washed with PBS to remove excess CuO@CNSs and lysed using cell lysis buffer. The mass of copper content was determined by ICP-MS.

Biocompatibility of CuO@CNSs
L929 and 4T1 cells were seeded into 96-well plates (6×10^3 cells per well) and cultured with different concentrations (0, 12.5, 25, 50, 100, and 200 μg mL^{-1}) of CuO@CNSs. After incubation overnight, standard 3-(4,5-di-methylthiazol-2-yl)-2,5-diphenyltetrazolium bromide (MTT) assay was used to measure the cell viability.

In vitro cytotoxicity detection
The cytotoxicity of CuO@CNSs-DOX was performed on 4T1 cells by the MTT test. 4T1 cells were seeded into 96-well plates (5×10^3 cells per well). After overnight incubation, fresh Dulbecco's modified Eagle medium (DMEM) containing CuO@CNSs, pure DOX or CuO@CNSs-DOX was added into the plates. The cells were washed with PBS after 4-h incubation, and then exposed to NIR light (2 W cm^{-2}) for 5 min. MTT assay was used to measure the cell viability.

Flow cytometry
Flow cytometry was also performed to analyze the cytotoxicity of CuO@CNSs-DOX. 4T1 cells were seeded into 6-well plates (3×10^5 cells per well) and incubated with CuO@CNSs and CuO@CNSs-DOX, respectively, and then exposed to 808 nm laser for 10 min. Annexin V-FITC and PI were used to stain the cells following the manufacturer's instructions (BestBio, Shanghai, China).

Animal experiments
All experiments of mice were approved by the Institutional Animal Care and Use Committee of Jilin University. Six–eight-week-old female Balb/c mice were purchased from the Center for Experimental Animals, Jilin University (Changchun, China).

IR and PA imaging
In vitro imaging was acquired by dissolution of CuO@CNSs in water with different concentrations. For *in vivo* imaging, 4T1-bearing mice were intratumorally injected with CuO@CNSs. IR thermal images and a pre-

clinical photoacoustic computed tomography scanner (Endra Nexus 128, USA) were used to obtain IR and PA imaging.

Anti-tumor experiment

Balb/c mice were injected with 4T1 cells in the left axilla. After 7 d, the tumor diameter reached 6–10 mm. The mice were randomly divided into six groups (six mice in each group): (i) PBS as control group; (ii) CuO@CNSs; (iii) CuO@CNSs+NIR; (iv) pure DOX; (v) CuO@CNSs-DOX; (vi) CuO@CNSs-DOX+NIR. The mice were intra-tumorally injected with the above materials and exposed to 808-nm NIR irradiation ($2\ \mathrm{W\ cm^{-2}}$, 10 min) after injection for 3 h. The tumor sizes and weights of mice were measured every two days, and the tumor volumes were calculated with the formula of $V=$(tumor length)×(tumor width)^2/2.

Biocompatibility *in vivo*

Mice were executed after tumor therapy. Major organs of the mice (heart, liver, spleen, lung and kidney) were collected, fixed in 4% polyformaldehyde, embedded in paraffin, sliced and stained with hematoxylin and eosin (H&E), and photographed using a biological microscope (BX-53, Olympus, Japan).

Statistical analysis

All the data were analyzed by the Statistical Program for Social Sciences software (SPSS, USA). All data were expressed as means (standard deviation), and statistical difference was considered to be present at $p<0.05$. Except as mentioned, all assays were repeated in triplicate in three independent experiments.

RESULTS AND DISCUSSION

Fabrication and characterization

The synthesis procedures and anti-cancer mechanism are illustrated in Scheme 1. The CNSs were synthesized *via* the solvothermal method [24]. The Cu^{2+} was adsorbed on the surface of CNSs and reacted with dissolved oxygen in water to produce CuO in vacuum. DOX was introduced to the surface of CuO@CNSs by electrostatic adsorption. Scanning electron microscopy (SEM) (Fig. 1a) and
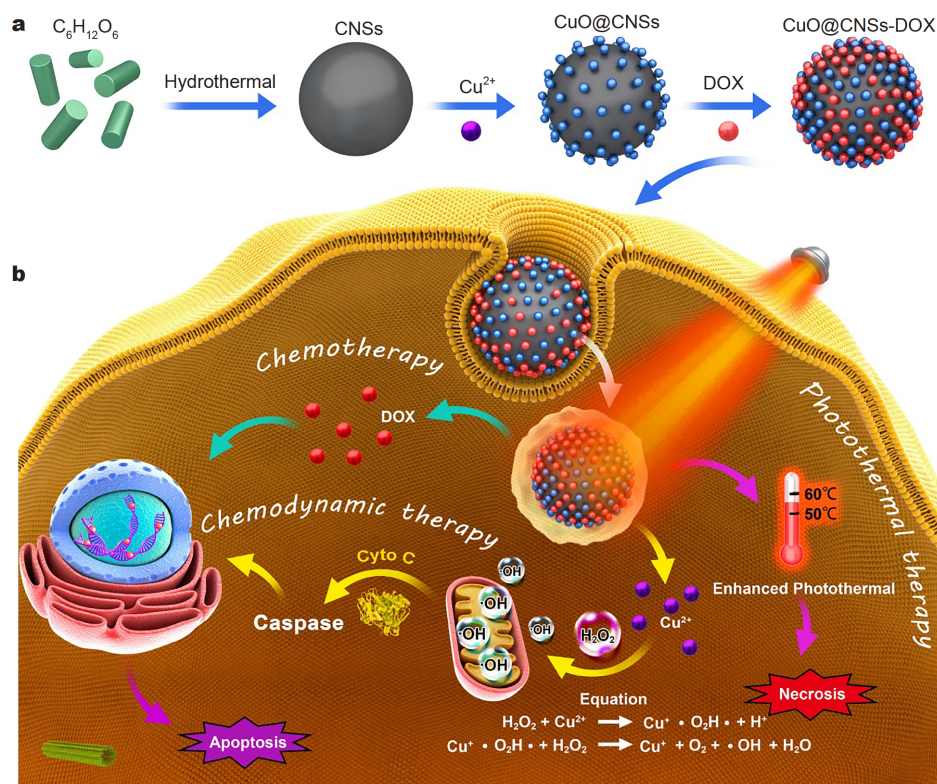
Scheme 1 (a) Schematic illustration of the preparation process of the CuO@CNSs-DOX nanoplatforms. CNSs were synthesized *via* the solvothermal method. CuO was adsorbed onto the CNSs, and DOX was loaded onto the surface of CuO@CNSs by electrostatic adsorption. (b) Schematic illustration of the endocytosis of CuO@CNSs-DOX nanoplatforms for PTT, CDT, and CT.

transmission electron microscopy (TEM) (Fig. 1b) images confirm that the CuO@CNSs have uniformed spherical structure with an average size of 150 nm. Fig. S1 displays that the hydrodynamic diameters of CuO@CNSs were 150–200 nm, which are suitable to accumulate in tumor cells *via* the enhanced permeability and retention (EPR) effect. In addition, the dynamic light scattering (DLS) diameters of CuO@CNSs dispersed in water, PBS, culture medium (DMEM) and fetal calf serum were tested to explore the stability of CuO@CNSs, respectively. As shown in Fig. S2a–d, these DLS diameters do not show any significant change after 3 d of storage, clearly demonstrating the stability of CuO@CNSs.

The structure of nanoparticles was verified by X-ray diffraction (XRD) (Fig. 1f). The wide-angle peak at 22° was the characteristic peak of CNSs and no defined diffraction peaks of CuO were observed [27], demonstrating that the nanoparticles have poor crystallinity. The elemental compositions of CuO@CNSs were detected by energy dispersive X-ray (EDX) mapping (Fig. 1c–e) and

X-ray photoelectron spectroscopy (XPS) (Fig. S3), proving that the elemental Cu was bound to CNSs. In Fig. 1h, the peak at 532.1 eV corresponded to O^{2-}. In Fig. 1g, peaks at 934 and 955 eV corresponded to Cu(II) $2p_{3/2}$ and Cu(II) $2p_{1/2}$, respectively. Two satellite peaks at 943 and 962 eV were the characteristic peaks of CuO [28]. These results confirmed that the Cu in the form of CuO was bound to carbon spheres. The evolution of zeta potential confirmed the successful modification in each preparation step (Fig. 2a). After decoration with negatively charged CuO, the zeta potential of nanoparticles decreased from −24.5 to −28.4 mV, and the zeta potential was increased to −19.4 mV after further adsorption of positively charged DOX. The specific surface areas of CNSs and CuO@CNSs *via* the N_2 adsorption and desorption were 33.37 $m^2 g^{-1}$ (Fig. 2b) and 43.307 $m^2 g^{-1}$ (Fig. 2c), respectively, confirming that there were no obvious changes in surface area before and after the adsorption of CuO.
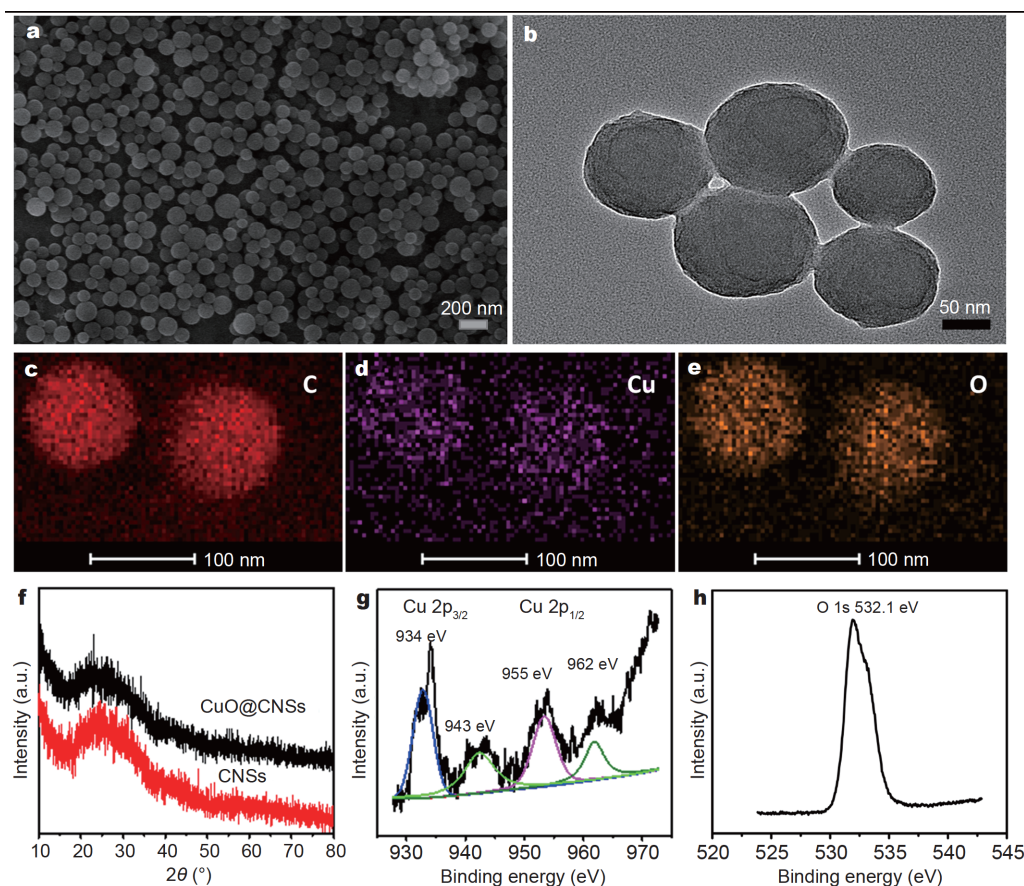
The functional groups of CuO@CNSs were identified

Figure 1 (a) SEM and (b) TEM images of CuO@CNSs. The elemental mappings of (c) C, (d) Cu, and (e) O of CuO@CNSs. (f) XRD patterns of CNSs and CuO@CNSs. XPS spectra of (g) Cu 2p and (h) O 1s.
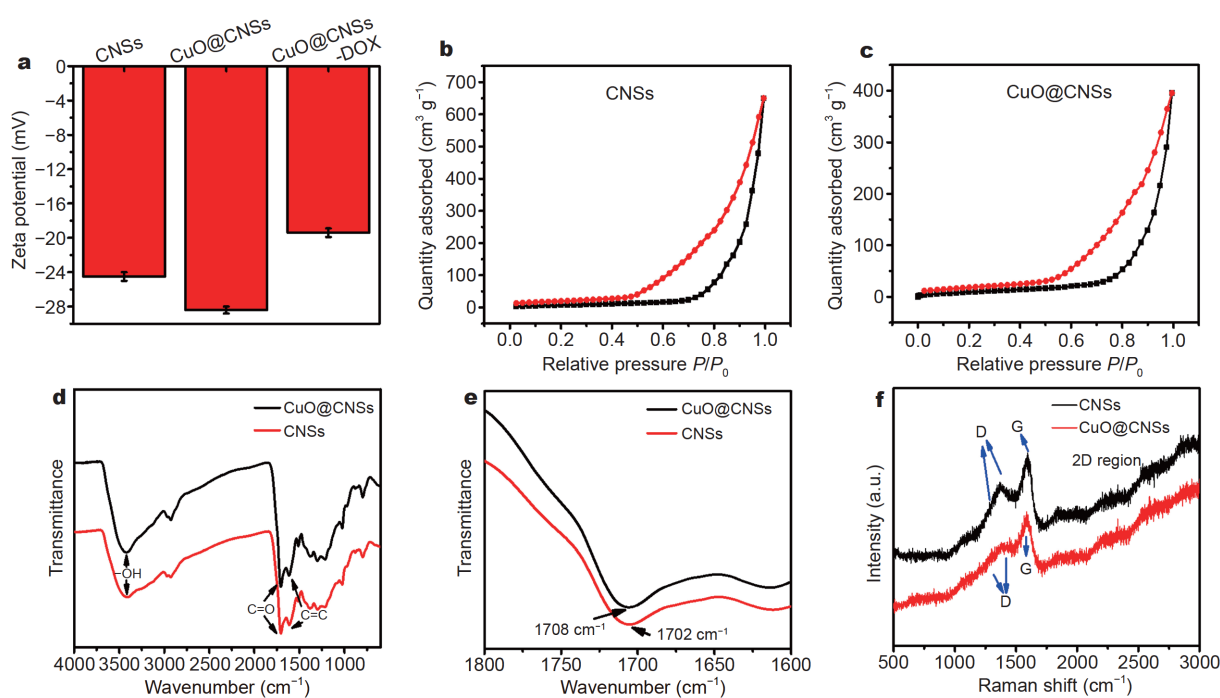
Figure 2 (a) Zeta potentials of CNSs, CuO@CNSs and CuO@CNSs-DOX dispersed in water. N_2 adsorption-desorption isotherms of (b) CNSs and (c) CuO@CNSs. (d) FTIR spectra of CNSs and CuO@CNSs with functional groups. (e) Expanded FTIR spectra of CNSs and CuO@CNSs in the wavenumber range of 1800–1600 cm^{-1}. (f) Raman spectra of CNSs and CuO@CNSs.

via Fourier transform infrared (FTIR) spectra. The connection between CuO and CNSs caused the movement of the peak from 1702 to 1708 cm^{-1} (Fig. 2e) [29]. Peaks at 3300–3500 cm^{-1} corresponded to the OH stretching (Fig. 2d), confirming that there were many hydroxyl groups on the surface of nanoparticles [30]. The above results indicate that the CuO@CNSs have good hydrophilicity. Raman spectra of CNSs and CuO@CNSs were also measured (Fig. 2f). The D peaks of CNSs located at 1340 and 1430 cm^{-1} shift to 1360 and 1450 cm^{-1} for CuO@CNSs, respectively. The red shift of the D peaks was due to the breathing of sp^2 rings caused by defects [31]. The G peak of CNSs located at 1603 cm^{-1} shifts to 1580 cm^{-1} for CuO@CNSs, which is due to the stretch of C sp^2 atoms. The above results also prove that the CuO nanoparticles were adsorbed onto CNSs [32–34].

The pH-sensitive release of Cu^{2+} and production of ·OH
CuO can release Cu^{2+} in an acidic environment. ICP-MS was used to detect the concentration of Cu^{2+} ions. We measured the release of Cu^{2+} at different pH (7.4, 6.5, and 5.0) (Fig. 3a), which corresponded to the blood environments (pH 7.4), tumor microenvironment (pH 6.5) and intracellular condition (pH 5), respectively [35]. Only

about 20% Cu^{2+} ions were released within 10 h at pH 7.4. About 40% and 80% copper ions were released at pH 6.5 and pH 5.0, respectively, which were almost two and four times as much as the amount of copper ions released at pH 7.4. The results confirmed that the release of copper ions was pH-dependent. SEM was used to observe the change of morphology at different pH (7.4, 6.5, and 5.0) (Fig. S4). With the decrease of pH, the morphology of the material was destroyed more seriously. The above results proved that the Cu^{2+} ions can be selectively released to tumor sites, which can alleviate the damage to normal tissues. It is generally known that the iron-initiated Fenton chemistry can kill tumor cells *via* converting endogenous H_2O_2 into ·OH [22]. Cu^{2+}-mediated Haber-Weiss and Fenton-like reactions to generate ·OH like Fe^{2+} were also reported [36]. Here, to verify the ·OH generation, TAOH, which can capture ·OH to produce strong fluorescent hydroxylation product 2-hydroxyterephthalic acid, was chosen to indirectly measure the amount of ·OH [37,38]. As exhibited in Fig. 3b, Cu^{2+} can produce ·OH by catalyzing hydrogen peroxide.

Electron spin resonance (ESR) technique was employed to monitor the ·OH production with 5,5′-dimethylpyrroline-1-oxide (DMPO) as the spin trap agent. As displayed in Fig. S5, the ESR signal of ·OH radical with
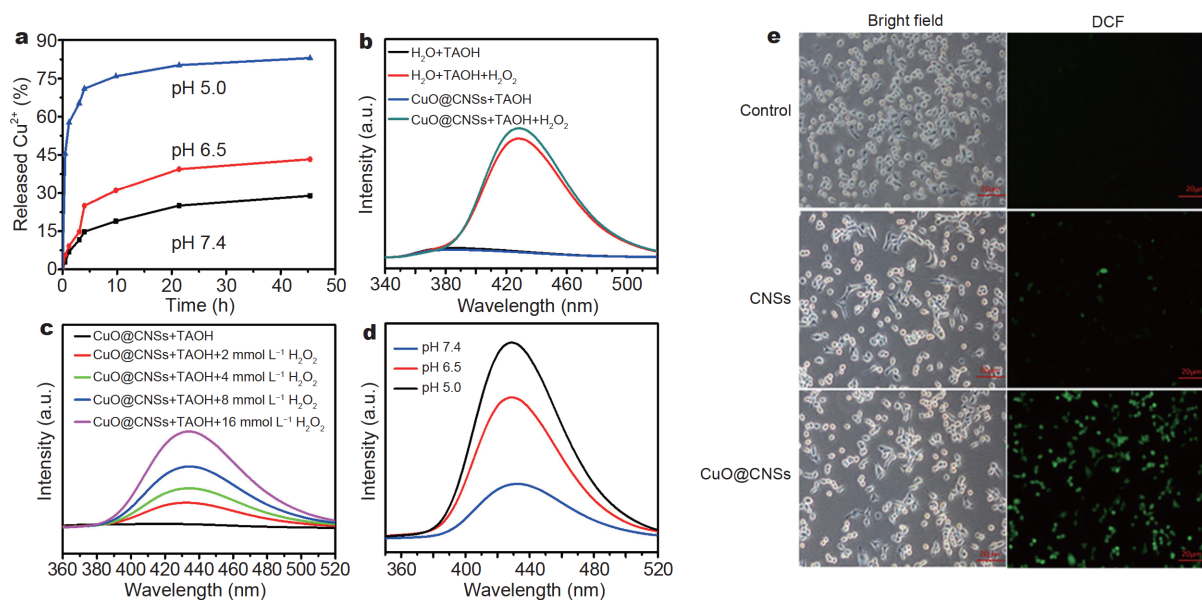
Figure 3 (a) The released Cu^{2+} from CuO@CNSs at different pH (7.4, 6.5, and 5.0). (b) The production of hydroxyl radicals in different solutions. (c) The production of hydroxyl radicals with different concentrations of H_2O_2 (0, 2, 4, 8, and 16 mmol L^{-1}). (d) The production of hydroxyl radicals at different pH (7.4, 6.5, and 5.0). (e) Intracellular production of hydroxyl radicals with different treatments, including control, CNSs and CuO@CNSs.

the typical peak intensity of 1:2:2:1 was observed in the CuO@CNSs and H_2O_2 mixed solution, further confirming the generation of ·OH. Besides, the ·OH generation was H_2O_2 concentration-dependent (Fig. 3c). With the increase of H_2O_2 concentration, the absorption intensity of TAOH increased, indicating that more ·OH radicals were generated. In addition, the ·OH generation was also pH-dependent (Fig. 3d). With the decrease of pH, more copper ions were released, which can produce more ·OH by Cu^{2+}-mediated Haber-Weiss and Fenton-like reactions.

2,7-Dichlorodihydrofluorescein (DCFH-DA) which can be oxidized to 2′,7′-dichlorofluorescein (DCF) with green fluorescence by the generated ·OH was used to examine the ·OH in 4T1 cells. As exhibited in Fig. 3e, stronger green fluorescence can be observed in CuO@CNSs group compared with the control and CNSs groups, confirming that more ·OH radicals were generated in cells via Cu^{2+} mediated Haber-Weiss and Fenton-like reactions.

Photothermal effects of CuO@CNSs
Compared with CNSs, the CuO@CNSs displayed enhanced NIR absorption and photothermal properties (Fig. 4a, b). The photothermal conversion efficiency (Fig. S6) of CuO@CNSs (10.14%) was also higher than that of CNSs (6.7%).

To find out the cause of photothermal enhancement, the band gap properties of CNSs and CuO@CNSs were calculated based on UV-Vis spectra. As shown in Fig. 4c, the values of band gap decreased from 1.09 to 1.03 eV after the adsorption of CuO. To further explore the reasons for photothermal enhancement, molecular models were constructed to calculate the change of the band gaps [39,40]. When CuO was adsorbed on CNSs, defects appeared on the surface of CNSs. DFT was employed to investigate the electronic structures of CNSs, defected CNSs, and CuO@CNSs, respectively, and the results are shown in Fig. 4d and Fig. S7a. There was a band gap near the Fermi level for CNSs, while it was reduced as the introduction of C defect. This result suggested that the defect in CNSs can improve the electronic transportation, which was the key factor to enhance the photothermal conversion efficiency of CNSs. However, the band gap disappeared when the CuO cluster was placed on the defect site. These results indicated that the CuO@CNSs showed higher photothermal conversion efficiency than CNSs, which was in agreement with the experimental observation. To further explore the mechanism of photothermal conversion of CuO@CNSs, the partial densities of state of C-2p and Cu-3d in the interface are revealed in Fig. S7b. The disappeared band gap was mainly from the C-2p and Cu-3d, which were overlapped near the Fermi level. It can be
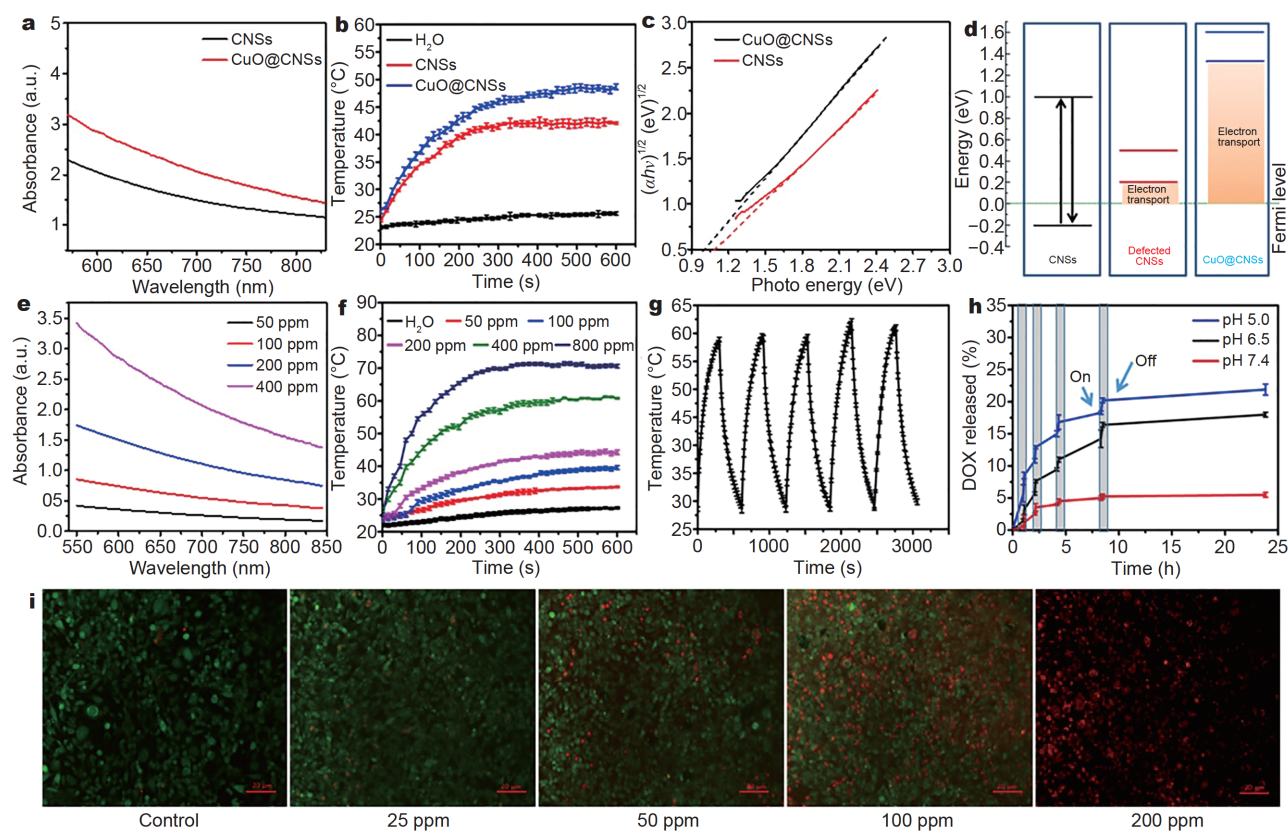
Figure 4 (a) The UV-Vis absorption spectra of CNSs and CuO@CNSs. (b) Temperature change curves of CNSs and CuO@CNSs with the same concentration under NIR irradiation (808 nm, 2 W cm^{-2}, 10 min). (c) Optical bandgaps of CNSs and CuO@CNSs. (d) The energy levels of CNSs, defected CNSs and CuO@CNSs. (e) UV-Vis absorption spectra of CuO@CNSs with different concentrations. (f) Temperature change curves of CuO@CNSs with different concentrations under NIR irradiation (808 nm, 2 W cm^{-2}, 10 min). (g) Temperature changes of the CuO@CNSs (400 ppm) over five On/Off cycles under 808-nm irradiation. (h) Released DOX from CuO@CNSs-DOX under 808-nm irradiation at different pH. (i) Fluorescence images of 4T1 cells co-stained with calcein-AM and PI after incubation with different concentrations of CuO@CNSs and irradiation with 808-nm NIR (2 W cm^{-2}) for 10 min.

deduced that the higher photothermal conversion efficiency of CuO@CNSs was due to the synergistic function between the Cu and C. Fig. 4e and f reveal that the NIR absorption and the photothermal effect of solution are concentration-dependent. The temperature of CuO@CNSs solution reached up to 60.3°C from 23°C when the concentration was 400 ppm, while water displayed mild temperature increase (less than 5°C). Besides, the photothermal effect of CuO@CNSs was stable (Fig. 4g). The above data proved that the CuO@ CNSs have potential to be photothermal agents [41].

To further explore the photothermal performance, calcein-AM and PI were used to stain cancer cells after NIR irradiation to distinguish the dead (red) and live (green) cells, respectively (Fig. 4i). With the increase of concentration, the number of dead cells increased. So the concentration-dependent cytotoxicity confirmed that the CuO@CNSs can be used for PTT.

DOX loading and releasing behavior
DOX was loaded on the surface of CuO@CNSs *via* electrostatic adsorption, with a loading efficiency of 12%. The cumulative drug release curves at different pH values are exhibited in Fig. 4h. 24% and 15% of DOX were released within 25 h at pH 5.0 and 6.5, respectively [42–44], which are almost five and three times as much as the amount of DOX released at pH 7.4. The result indicated that the release of DOX was pH-dependent. When exposed to 808-nm laser irradiation for 10 min (2 W cm^{-2}), a burst and quick release of DOX was observed. But when the laser was shut off, the release rate immediately decreased. Importantly, the rapid release of DOX under NIR irradiation was attributed to the good photothermal effect of the CuO@CNSs.

Celluar uptake assays
Fluorescence microscope and ICP-MS were used to in-

vestigate the cellular uptake of the NPs. As shown in Fig. 5a, the endocytosis process was time-dependent and DOX gradually accumulated in cells with the increase of time. To further investigate the accumulation of nanoparticles in cells, ICP-MS was used to explore the concentrations of copper ions internalized by 4T1 cells at different time points (10, 60 and 240 min). In Fig. 5b, the contents of copper in 4T1 cells after incubation with CuO@CNSs at 10, 60 and 240 min were 9.88, 54.51 and 73.71 ng Cu per 10^5 cells, respectively.

In vitro cytotoxicity of CuO@CNSs

The biocompatibility of CuO@CNSs was measured by the standard MTT assay. We studied the viabilities of 4T1 and L929 cells after incubation with CuO@CNSs at different concentrations. In Fig. 5e, the viability of the L929 cells was greater than 90% at the concentration of as high as 200 ppm, but when 4T1 cells were incubated with the same concentration, the viability decreased to 65%. The different survival rates were caused by the different H_2O_2 contents between 4T1 and L929 cells [22].

The cytotoxicity of CuO@CNSs against 4T1 cells was also measured by the MTT assay. After incubation with CuO@CNSs, CuO@CNSs+NIR, pure DOX, CuO@CNSs-DOX or CuO@CNSs-DOX+NIR for 24 h, the cell viabilities are shown in Fig. 5c. The viability of the cells treated with CuO@CNSs alone was 65% at the concentration of 200 ppm, but when treated with CuO@CNSs+NIR at the same concentration, the viability decreased to 50%, demonstrating the good photothermal effect of the CuO@CNSs. It is notable that the cells cultured with CuO@CNSs-DOX+NIR have the lowest cell viability of 18% compared with the other groups. The above results confirm that the multi-mode therapy has a better anti-tumor effect.

The apoptosis ratio of 4T1 cells after different treatments was detected by flow cytometry (Fig. 5d). The CuO@CNSs-DOX+NIR group displayed 29% of cell apoptosis, which is higher than CuO@CNSs-DOX (5.44%), DOX (19.64%), CuO@CNSs+NIR (21.02%) and CuO@CNSs (8.98%) groups, respectively. The above results proved that the multi-mode therapy can promote
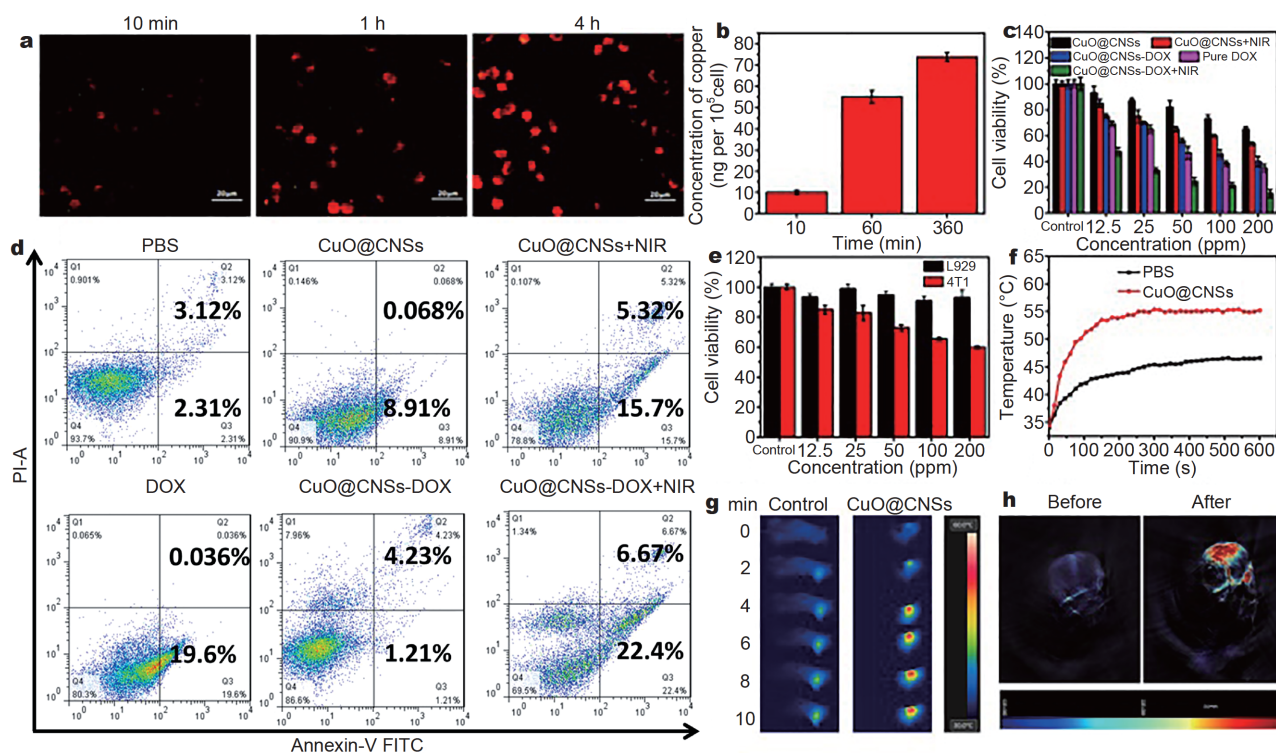

Figure 5 (a) Cellular uptake of CuO@CNSs-DOX in 4T1 cells at different time points (10 min, 1 h, and 4 h). (b) Mass of copper internalized in 4T1 cells after incubation with CuO@CNSs at different time points (10 min, 1 h, and 4 h). (c) The cell viability of 4T1 cells after various treatments, where the cells were exposed to 808-nm laser (2 W cm^{-2}) for 5 min or not. (d) Flow cytometric analyses of cell apoptosis. (e) The cell viability of 4T1 and L929 cells incubated with CuO@CNSs. (f) Temperature plot and (g) the IR thermal images of 4T1 tumor-bearing mice after intratumoral injection of CuO@CNSs (5 mg mL^{-1}, 0.1 mL) for 3 h and exposed to 808-nm laser (2 W cm^{-2}, 10 min). (h) PA images of tumor site before and after injection with CuO@CNSs.

apoptosis and improve treatment efficiency.

IR and PA bioimaging

The *in vivo* IR thermal images of Balb/c mice injected with or without CuO@CNSs were taken. Fig. 5g and f show the surface temperature of the tumor was quickly increased by 20°C when the mice were treated with CuO@CNSs and irradiated with 808-nm laser (2 W cm^{-2}, 10 min), which was much higher than the control group (increase of 10°C). PA imaging, as a newly emerging bioimaging method, can provide noninvasive diagnosis of diseases based on ultrasound emission. The intensity of PA signal was related to the absorption strength of nanomaterials. As shown in Fig. S8, a good linear relationship was observed between the PA signal and nanoparticles concentration *in vitro*, suggesting that the CuO@CNSs can be used as an ideal PA imaging contrast agent for imaging-guided cancer diagnosis. For *in vivo* PA imaging (Fig. 5h), the tumor region showed weak PA signals before injection, but when the mice were intratumorally injected with CuO@CNSs, the tumor region showed strong PA signals. The above results verified that CuO@CNSs were good contrast agents to offer guidance for determining the time window of tumor treatment [45–47].

In vivo antitumor efficacy

The *in vivo* antitumor effect was explored by a 4T1 tumor-bearing Balb/c mice model. First, we divided the tumor-bearing Balb/c mice into six groups (six mice in each group): (i) PBS (0.1 mL) only; (ii) CuO@CNSs (5 mg mL^{-1}, 0.1 mL); (iii) CuO@CNSs+NIR (5 mg mL^{-1}, 0.1 mL, 808+, 10 min); (iv) DOX (680 μg mL^{-1}, 0.1 mL); (v) CuO@CNSs-DOX (5 mg mL^{-1}, 0.1 mL); (vi) CuO@CNSs-DOX+NIR (5 mg mL^{-1}, 0.1 mL, 808+, 10 min). The tumor sizes and weights of the mice were measured every two days. As shown in Fig. 6a, tumors treated with PBS or CuO@CNSs showed negligible anticancer effect. Tumors treated with CuO@CNSs+NIR, CuO@CNSs-DOX or DOX exhibited moderate therapeutic effect. It is notable that when the mice were treated with CuO@CNSs-DOX+NIR, the growth of tumor was obviously inhibited, suggesting that the three-mode therapy has an excellent effect. In Fig. 6b, there are no obvious changes of the body weights of mice. All of mice were sacrificed and the tumors were stripped at Day 16. As presented in Fig. 6c, the photographs show that the CuO@CNSs-DOX+NIR group has the best anti-cancer effect. The H&E staining images of main organ slices of mice (heart, liver, spleen, lung, and kidney) were photographed after different treatments. As presented in
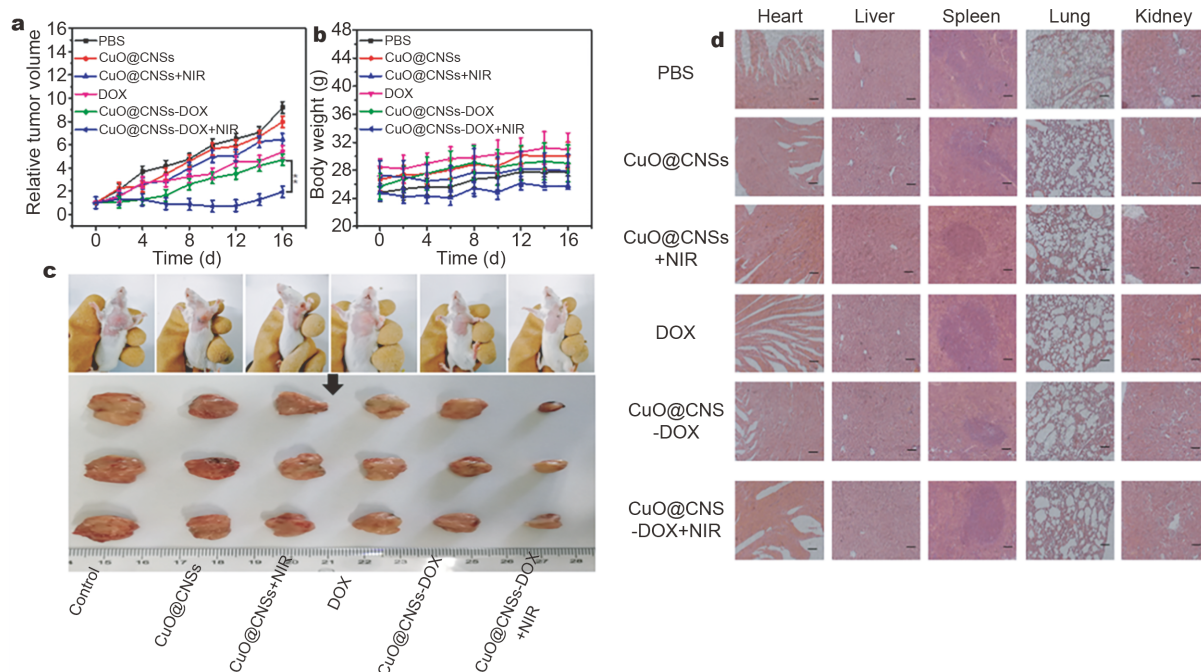

Figure 6 (a) Relative tumor volumes. (b) Body weights of Balb/c mice after various treatments. The mice were intratumorally injected with nanoparticles (5 mg mL^{-1}, 0.1 mL) and irradiated with 808-nm laser (2 W cm^{-2}, 10 min). (c) Photographs of mice and tumors after various treatments. (d) H&E staining images of the main organ slices of mice after various treatments. Scale bar is 20 μm. ** $p<0.01$.

Fig. 6d, neither organ damage nor inflammatory lesion was detected, which proved the low toxicity of CuO@CNSs-DOX *in vivo*. These results indicated that the multifunctional CuO@CNSs-DOX nanoplatforms have a high biosafety and anti-cancer effect.

CONCLUSIONS

In summary, we successfully synthesized multifunctional nanoplatforms CuO@CNSs-DOX to realize the combination therapy of PTT, CDT, and CT. CuO was adsorbed on the surface of CNSs, which improved the photothermal conversion efficiency of nanoparticles from 6.7% to 10.14%. The enhancement of photothermal conversion efficiency was due to the electron transitions between C-2p and Cu-3d. In addition, CuO was also a CDT agent, which can release Cu^{2+} at the tumor site to produce ·OH *via* Haber-Weiss and Fenton-like reactions. Chemotherapeutic drug DOX was loaded on the surface of CuO@CNSs *via* electrostatic adsorption and released quickly at the tumor site to kill cancer cells. Besides, CuO@CNSs can be used for the IR/PA dual-modal imaging to provide the real-time diagnosis for diseases. The excellent anti-tumor effect and high biosafety make the multi-mode nanoplatforms have great potential in biomedical applications.

1   Taratula O, Doddapaneni BS, Schumann C, *et al.* Naphthalocyanine-based biodegradable polymeric nanoparticles for image-guided combinatorial phototherapy. Chem Mater, 2015, 27: 6155–6165

2   Jing Z, Zhan J. Fabrication and gas-sensing properties of porous ZnO nanoplates. Adv Mater, 2008, 20: 4547–4551

3   Cheng L, Liu J, Gu X, *et al.* PEGylated WS_2 nanosheets as a multifunctional theranostic agent for *in vivo* dual-modal CT/photoacoustic imaging guided photothermal therapy. Adv Mater, 2014, 26: 1886–1893

4   Ge J, Jia Q, Liu W, *et al.* Red-emissive carbon dots for fluorescent, photoacoustic, and thermal theranostics in living mice. Adv Mater, 2015, 27: 4169–4177

5   Mao F, Wen L, Sun C, *et al.* Ultrasmall biocompatible Bi_2Se_3 nanodots for multimodal imaging-guided synergistic radio-photothermal therapy against cancer. ACS Nano, 2016, 10: 11145–11155

6   Robinson JT, Tabakman SM, Liang Y, *et al.* Ultrasmall reduced graphene oxide with high near-infrared absorbance for photothermal therapy. J Am Chem Soc, 2011, 133: 6825–6831

7   Zhu X, Feng W, Chang J, *et al.* Temperature-feedback upconversion nanocomposite for accurate photothermal therapy at facile temperature. Nat Commun, 2016, 7: 10437

8   Xiang Y, Li N, Guo L, *et al.* Biocompatible and pH-sensitive MnO-loaded carbonaceous nanospheres (MnO@CNSs): A theranostic agent for magnetic resonance imaging-guided photothermal therapy. Carbon, 2018, 136: 113–124

9   Nandi S, Bhunia SK, Zeiri L, *et al.* Bifunctional carbon-dot-WS_2 nanorods for photothermal therapy and cell imaging. Chem Eur J, 2017, 23: 963–969

10   Liu Y, Zhen W, Jin L, *et al.* All-in-one theranostic nanoagent with enhanced reactive oxygen species generation and modulating tumor microenvironment ability for effective tumor eradication. ACS Nano, 2018, 12: 4886–4893

11   Xu C, Wang Y, Yu H, *et al.* Multifunctional theranostic nanoparticles derived from fruit-extracted anthocyanins with dynamic disassembly and elimination abilities. ACS Nano, 2018, 12: 8255–8265

12   Feng L, Xie R, Wang C, *et al.* Magnetic targeting, tumor microenvironment-responsive intelligent nanocatalysts for enhanced tumor ablation. ACS Nano, 2018, 12: 11000–11012

13   Hureau C, Faller P. Aβ-mediated ROS production by Cu ions: Structural insights, mechanisms and relevance to Alzheimer's disease. Biochimie, 2009, 91: 1212–1217

14   Laggner H, Hermann M, Gmeiner BMK, *et al.* Cu^{2+} and Cu^+ bathocuproine disulfonate complexes promote the oxidation of the ROS-detecting compound dichlorofluorescin (DCFH). Anal Bioanal Chem, 2006, 385: 959–961

15   Rehman SU, Zubair H, Sarwar T, *et al.* Redox cycling of Cu(II) by 6-mercaptopurine leads to ROS generation and DNA breakage: Possible mechanism of anticancer activity. Tumour Biol, 2015, 36: 1237–1244

16   Ding B, Shao S, Jiang F, *et al.* MnO_2-disguised upconversion hybrid nanocomposite: An ideal architecture for tumor microenvironment-triggered UCL/MR bioimaging and enhanced chemodynamic therapy. Chem Mater, 2019, 31: 2651–2660

17   Assal ME, Shaik MR, Kuniyil M, *et al.* Ag_2O nanoparticles/$MnCO_3$, $-MnO_2$ or $-Mn_2O_3$/highly reduced graphene oxide composites as an efficient and recyclable oxidation catalyst. Arabian J Chem, 2019, 12: 54–68

18   Wan SS, Cheng Q, Zeng X, *et al.* A Mn(III)-sealed metal-organic framework nanosystem for redox-unlocked tumor theranostics. ACS Nano, 2019, 13: 6561–6571

19   Park J, Lim DH, Lim HJ, *et al.* Size dependent macrophage responses and toxicological effects of Ag nanoparticles. Chem Commun, 2011, 47: 4382

20   Zhang X, Xi Z, Machuki JO, *et al.* Gold cube-in-cube based oxygen nanogenerator: A theranostic nanoplatform for modulating tumor microenvironment for precise chemo-phototherapy and multimodal imaging. ACS Nano, 2019, 13: 5306–5325

21   Liu B, Li C, Chen G, *et al.* Synthesis and optimization of MoS_2@Fe_3O_4-ICG/Pt(IV) nanoflowers for MR/IR/PA bioimaging and combined PTT/PDT/chemotherapy triggered by 808 nm laser. Adv Sci, 2017, 4: 1600540

22   Wu C, Wang S, Zhao J, *et al.* Biodegradable Fe(III)@WS_2-PVP nanocapsules for redox reaction and TME-enhanced nanocatalytic, photothermal, and chemotherapy. Adv Funct Mater, 2019, 29: 1901722

23   Liu Y, Jia Q, Guo Q, *et al.* Simultaneously activating highly selective ratiometric MRI and synergistic therapy in response to intratumoral oxidability and acidity. Biomaterials, 2018, 180: 104–116

24   Miao ZH, Wang H, Yang H, *et al.* Glucose-derived carbonaceous nanospheres for photoacoustic imaging and photothermal therapy. ACS Appl Mater Interfaces, 2016, 8: 15904–15910

25   Zhao M, Li B, Wang P, *et al.* Supramolecularly engineered NIR-II

and upconversion nanoparticles *in vivo* assembly and disassembly to improve bioimaging. Adv Mater, 2018, 30: 1804982

26 Fan Y, Wang S, Zhang F. Optical multiplexed bioassays for improved biomedical diagnostics. Angew Chem Int Ed, 2019, 58: 13208–13219

27 Chen Z, Jiao Z, Pan D, *et al.* Recent advances in manganese oxide nanocrystals: Fabrication, characterization, and microstructure. Chem Rev, 2012, 112: 3833–3855

28 Kung ML, Tai MH, Lin PY, *et al.* Silver decorated copper oxide (Ag@CuO) nanocomposite enhances ROS-mediated bacterial architecture collapse. Colloids Surfs B-Biointerfaces, 2017, 155: 399–407

29 Yumoto F, Nara M, Kagi H, *et al.* Coordination structures of Ca^{2+} and Mg^{2+} in Akazara scallop troponin C in solution. Eur J Biochem, 2001, 268: 6284–6290

30 Chen YW, Su YL, Hu SH, *et al.* Functionalized graphene nanocomposites for enhancing photothermal therapy in tumor treatment. Adv Drug Deliver Rev, 2016, 105: 190–204

31 Ferrari AC, Robertson J. Interpretation of Raman spectra of disordered and amorphous carbon. Phys Rev B, 1999, 61: 14095–14107

32 Sobon G, Sotor J, Jagiello J, *et al.* Graphene oxide *vs.* reduced graphene oxide as saturable absorbers for Er-doped passively mode-locked fiber laser. Opt Express, 2012, 20: 19463–19473

33 Guo S, Lu G, Qiu S, *et al.* Carbon-coated MnO microparticulate porous nanocomposites serving as anode materials with enhanced electrochemical performances. Nano Energy, 2014, 9: 41–49

34 Li J, Song Y, Ma Z, *et al.* Preparation of polyvinyl alcohol graphene oxide phosphonate film and research of thermal stability and mechanical properties. Ultrasons Sonochem, 2018, 43: 1–8

35 Mi P, Kokuryo D, Cabral H, *et al.* A pH-activatable nanoparticle with signal-amplification capabilities for non-invasive imaging of tumour malignancy. Nat Nanotech, 2016, 11: 724–730

36 Li M, Wang Y, Lin H, *et al.* Hollow CuS nanocube as nanocarrier for synergetic chemo/photothermal/photodynamic therapy. Mater Sci Eng-C, 2019, 96: 591–598

37 Huang CX, Chen HJ, Li F, *et al.* Controlled synthesis of upconverting nanoparticles/CuS yolk-shell nanoparticles for *in vitro* synergistic photothermal and photodynamic therapy of cancer cells. J Mater Chem B, 2017, 5: 9487–9496

38 Zhang MK, Wang XG, Zhu JY, *et al.* Double-targeting explosible nanofirework for tumor ignition to guide tumor-depth photothermal therapy. Small, 2018, 14: 1800292

39 Kresse G, Hafner J. *Ab initio* molecular-dynamics simulation of the liquid-metal-amorphous-semiconductor transition in germanium. Phys Rev B, 1994, 49: 14251–14269

40 Perdew JP, Burke K, Ernzerhof M. Generalized gradient approximation made simple. Phys Rev Lett, 1996, 77: 3865–3868

41 Yong Y, Cheng X, Bao T, *et al.* Tungsten sulfide quantum dots as multifunctional nanotheranostics for *in vivo* dual-modal image-guided photothermal/radiotherapy synergistic therapy. ACS Nano, 2015, 9: 12451–12463

42 Liang S, Xie Z, Wei Y, *et al.* DNA decorated Cu_9S_5 nanoparticles as NIR light responsive drug carriers for tumor chemo-phototherapy. Dalton Trans, 2018, 47: 7916–7924

43 Song G, Wang Q, Wang Y, *et al.* A low-toxic multifunctional nanoplatform based on $Cu_9S_5@mSiO_2$ core-shell nanocomposites: Combining photothermal- and chemotherapies with infrared thermal imaging for cancer treatment. Adv Funct Mater, 2013, 23: 4281–4292

44 Chen Y, Hou Z, Liu B, *et al.* DOX-$Cu_9S_5@mSiO_2$-PG composite fibers for orthotopic synergistic chemo- and photothermal tumor therapy. Dalton Trans, 2015, 44: 3118–3127

45 Lei Z, Sun C, Pei P, *et al.* Stable, wavelength-tunable fluorescent dyes in the NIR-II region for *in vivo* high-contrast bioimaging and multiplexed biosensing. Angew Chem Int Ed, 2019, 58: 8166–8171

46 Zhou L, Fan Y, Wang R, *et al.* High-capacity upconversion wavelength and lifetime binary encoding for multiplexed biodetection. Angew Chem Int Ed, 2018, 57: 12824–12829

47 Wang S, Liu L, Fan Y, *et al.* *In vivo* high-resolution ratiometric fluorescence imaging of inflammation using NIR-II nanoprobes with 1550 nm emission. Nano Lett, 2019, 19: 2418–2427

Author contributions Jiang F performed the experiments and wrote the draft of manuscript; Ding B, Zhao Y and Liang S helped with the design of cell and animal experiments; Cheng Z, Xing B and Teng B provided suggestions and comments on the manuscript; Ma P and Lin J proposed the project and revised the manuscript.

Conflict of interest The authors declare that they have no conflict of interest.

Supplementary information Experimental details and supporting data are available in the online version of the paper.

Fan Jiang received her BSc degree in chemistry from Zhengzhou University (ZZU) in 2017. She is currently a doctoral student under the supervision of Prof. Jun Lin at Changchun Institute of Applied Chemistry (CIAC), Chinese Academy of Sciences (CAS), and University of Science and Technology of China. Her research focuses on the development of inorganic nanoparticles for cancer therapy.

Ping'an Ma received his BSc degree in biology in 2005 and PhD degree in biochemistry in 2010, respectively, from Northeast Normal University. He is currently an assistant professor in Prof. Jun Lin's group at CIAC, CAS. His research focuses on the synthesis and application of multifunctional inorganic nanoparticles for bioapplication, particularly the design and mechanism of platinum-based anticancer drugs.

Jun Lin received BSc and MSc degrees in inorganic chemistry from Jilin University in 1989 and 1992, respectively, and a PhD degree (inorganic chemistry) from CIAC, CAS in 1995. He is currently a professor at CIAC, CAS. His research interests include luminescent materials and multifunctional composite materials as well as their applications in display, lighting and biomedical fields.

CuO修饰的碳纳米平台用于多重成像和联合增强的抗肿瘤治疗

姜帆[1,2], 丁彬彬[1,2], 赵雅洁[1,2], 梁双[1,2], 程子泳[1,2], 邢本刚[3], 滕博[4], 马平安[1,2*], 林君[1,2*]

摘要 将多功能纳米平台的设计合成应用于肿瘤的联合治疗得到研究人员的广泛关注. 本研究通过水热法制备了形貌均匀的光热材料碳纳米球，表面负载CuO和抗癌药盐酸阿霉素(DOX)实现光热/化学动力/化疗联合治疗. CuO通过静电吸附负载在碳纳米球(CNSs)表面，电子在C-2p与Cu-3d之间的跃迁提高了材料的光热转换效率. CuO也可以作为化学动力试剂，在肿瘤部位释放Cu^{2+}并通过Haber-Weiss和类Fenton反应产生羟基自由基诱导肿瘤细胞凋亡. DOX吸附在CuO@CNSs表面，表现出pH响应释放和近红外激光刺激响应的释放效果. 研究结果表明，CuO@CNSs-DOX纳米平台在体内外都有很好的抗癌效果，在肿瘤治疗方面有很大的应用潜力.